materials

MDPI

Article

Preparation of CeO_2/UiO-66-NH_2 Heterojunction and Study on a Photocatalytic Degradation Mechanism

Ziwei Liu, Yanli Zhuang *, Limin Dong *, Hongxu Mu, Shuo Tian, Leiming Wang and Aoxiang Huang

Heilongjiang Provincial Key Laboratory of CO_2 Resource Utilization and Energy Catalytic Materials, School of Material Science and Chemical Engineering, Harbin University of Science and Technology, Harbin 150040, China; liuziwei199604@163.com (Z.L.); hrbust_mhx@163.com (H.M.); tianshuo199606@163.com (S.T.); wangleiming199905@163.com (L.W.); hover1002@163.com (A.H.)
* Correspondence: zhuangyanli@hrbust.edu.cn (Y.Z.); donglm@hrbust.edu.cn (L.D.)

Abstract: CeO_2/UiO-66-NH_2 (marked as Ce/UN) composites were in-situ synthesized by a hydrothermal method. The properties, photocatalytic aspects, and degradation mechanism of Ce/UN were studied carefully. SEM results show that Ce/UN have a 3D flower-like structure, where octahedral UiO-66-NH_2 nanoparticles are embedded in the two-dimensional sheet of CeO_2. TEM results demonstrate that CeO_2 and UiO-66-NH_2 are bonded interfacially to constitute a hetero-junction construction. Data obtained by electrochemical impedance spectroscopy and fluorescence spectroscopy established that Ce/UN has less charge shift resistance and luminescence intensity than these of two pure substances. When the ratio of Ce/UN is 1:1, and the calcination temperature 400 °C is used, the degradation efficiency of RhB in photocatalysis by obtained Ce/UN is about 96%, which is much higher than in the case of CeO_2 (4.5%) and UiO-66-NH_2 (54%). The improved photocatalytic properties of Ce/UN may be due to the formation of hetero-junction, which is conducive for most photo-carriers and thus the interfacial charge shift efficiency is enhanced. By the free radical capture test, it can be inferred that the major active substances involved in the degradation related to photocatalysis is H^+ and $\cdot O_2^-$.

Keywords: CeO_2; UiO-66-NH_2; heterojunction; photocatalytic mechanism

Citation: Liu, Z.; Zhuang, Y.; Dong, L.; Mu, H.; Tian, S.; Wang, L.; Huang, A. Preparation of CeO_2/UiO-66-NH_2 Heterojunction and Study on a Photocatalytic Degradation Mechanism. *Materials* **2022**, *15*, 2564. https://doi.org/10.3390/ma15072564

Academic Editor: Haralampos N. Miras

Received: 17 February 2022
Accepted: 24 March 2022
Published: 31 March 2022

1. Introduction

Fast industry development in the last few decades leads to increased environmental pollution, which has to be solved, whereas renewable sources and environmental problems have attracted a lot of attention by the researchers [1–4]. The research on environment-friendly and sustainable energy composite materials will become an important research direction in the future. Rare earth oxides have the advantages of low price, stability and non-toxicity and in the light catalysis, batteries, and other fields have a wide range of applications [5,6]. Cerium oxide (CeO_2) has good conductivity and stability, and has high oxygen storage capacity because of the existence of reversible REDOX pairs of Ce^{3+}/Ce^{4+}, which enables it to have strong electronic interaction with other components at the interface [7]. Therefore, it has potential application as a carrier material in catalytic oxidation reactions. However, cerium oxide has a wide band gap and limited absorption of visible light, and its photoelectron generation and hole recombination rates are high, leading to its poor photocatalytic degradation performance [8,9]. Numerous researchers have stated that photocatalytic properties of materials can be improved by improving morphology, crystal plane regulation, substance doping, or heterojunction construction [7,10]. For example, Wu and Shen [11,12] prepared CeO_2/Co_3O_4 composite materials by a biological template method and solvothermal method, and improved the electron transmit rate of the materials by regulating the morphology of the composite materials. Pu and Chae [13,14] prepared Cu_2O/CeO_2 composite materials by calcination and sol-gel electrostatic spinning. By constructing p-n junction, the absorption of CeO_2 under visible light and separation efficiency

of a light carrier were improved. Other researchers prepared CdS/CeO_2 composites by two-step hydrothermal method, one-pot method, and solvothermal method, and improved the photocatalytic performance of the composites by constructing appropriate band gap matching [15–17].

Metal-organic framework compounds (MOFs), as a new type of substance different from semiconductors, have great potential in photocatalytic reactions because of their high specific regions on the surface, flexible porous size and design of internal construction [18–20]. As a photocatalytic agent, it can provide an additional pathway for photoelectron migration, thereby boosting the segregation of electrons and holes (e^-–h^+), in turn, improving the efficiency of composites in terms of photocatalysis. However, poor electrical conductivity, intrinsic catalytic activity, and stability affect its application in catalytic reactions. Researchers synthesized UiO-66-NH_2 MOFs with BiOBr [21,22], Ag_3PO_4 [23], CdS [24–26], and other semiconductor materials to structure a composite. The results show that the heterojunction structure is formed at the interface between MOFs and semiconductor substances, which can effectively inhibit the rapid restructuring of e^-–h^+, thus improving the properties of semiconductor substance in terms of photocatalysis [27,28].

Considering the low efficiency in photocatalysis, poor adsorption capacity, and low utilization rate of visible light of CeO_2, this paper intends to promote the separation efficiency of e^-–h^+ by constructing heterojunction. Meanwhile, the big specific surface areas of MOFs is used to improve the adsorption capacity of pure substances, and finally realize the improvement of the photocatalytic degradation performance of the material. Therefore, Ce/UN composite photocatalytic material was in-situ synthesized by a hydrothermal method in this paper, mainly studying the influence of preparation process and composite ratio on the photocatalytic degradation performance of composite materials, and revealing the photocatalytic degradation mechanism.

2. Materials and Experimental Procedures

All chemicals and reagents used in this paper are analytical grade reagents, bought from Shanghai Maclean Biochemical Technology Co., Ltd. (Shanghai, China), and have not been more purified.

2.1. Preparation of CeO_2 Nanosheets

Furthermore, 1.39 g $Ce(NO_3)_3$•$6H_2O$ and 0.75 g NH_4HCO_3 were separately dissolved in 200 mL deionized water. Then, the NH_4HCO_3 liquor was quickly poured into the $Ce(NO_3)_3$•$6H_2O$ solution and kept at 0 °C for 30 min. The mixed solution was filtered through a funnel to collect the products and washed with deionized water 3 times. The collected precipitate was dried at 69 °C for 4 h to get the precursor of CeO_2. Finally, the precursor of CeO_2 was calcined at 350 °C, 400 °C and 450 °C for 4 h to obtain CeO_2 nanosheets. The preparation process of CeO_2 nanosheets is according to Figure 1.

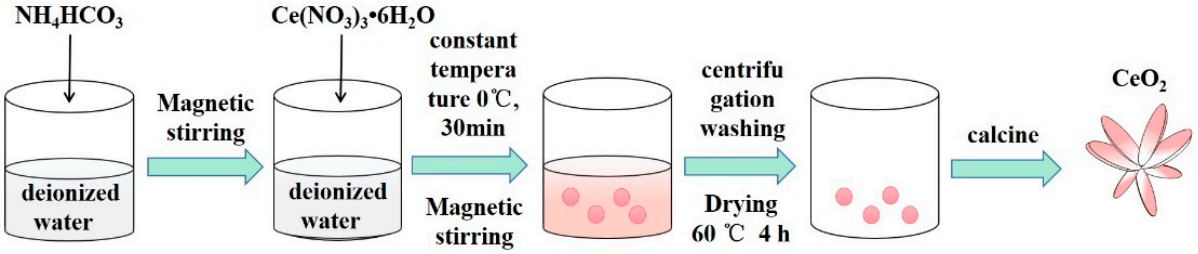

Figure 1. Diagrammatic sketch of the synthesis of CeO_2 nanosheets.

2.2. Preparation of Ce/UN Composites

Ultrasonic dispersion of 20.4 mg ZrCl4 and 14.5 mg 2-amino-1, 4-carboxylic acid in 10 mL dimethylformamide and 1.2 mL acetic acid mixed solvent, the prepared CeO_2

nanosheets were dissolved in the mixed solvent, and then the mixed solution was loaded into the teflon lined hydrothermal autoclave. It was kept warm for 12 h at 120 °C, and then centrifuged it three times with deionized water. The lamellar Ce/UN composite photocatalytic material was prepared by drying for 12 h at 60 °C. The preparation process of Ce/UN composites is referring to Figure 2. Synthetic quality ratio of 0.5:1, 1:1, 1.5:1, and 2:1 Ce/UN substance labels were 0.5-Ce/UN, 1-Ce/UN,1.5-Ce/UN, and 2-Ce/UN.

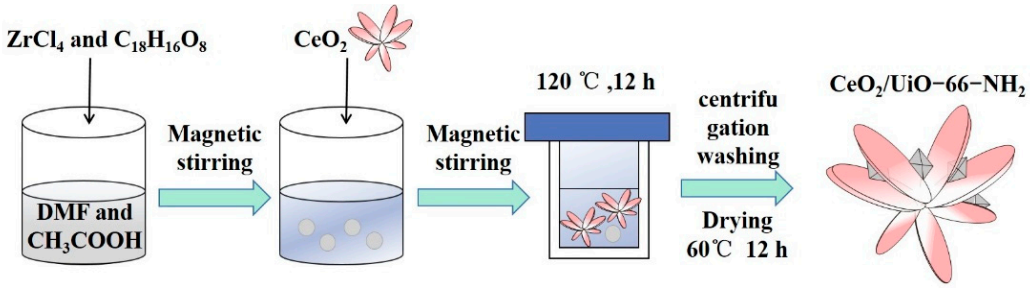

Figure 2. Diagrammatic sketch of the synthesis of Ce/UN composites.

2.3. Properties Characterization

The phase of the substance was characterized by a Model D/MAX-3B X-ray diffractometer (λ = 0.154 nm) manufactured by Tokyo Company, Japan. The diffraction target of the instrument was Cu-Ka (scanning rate was 4°/min), and the scanning Angle 2θ ranged from 10° to 80°. FEI Sirion200 (scanning electron microscopy, SEM, FEI Company, Hillsboro, FL, USA) was employed in looking into the microstructure and size of the material. The crystal structure and lattice spacing of photocatalytic substances were featured by transmission electron microscopy (TEM, JEM2100, JEOL, Showa, Japan). X-ray photoelectron spectroscopy (XPS, Thermo Escalab 250Xi, Thermo Fisher, Waltham, MA, USA) was used to determine the composition of the material. The surface area of the catalyst and the pore size distribution was measured using a Brunauer–Emmett–Teller surface area analyzer (BET, Micromeritics ASAP 2460, Micromeritics Instrument Corp, Shanghai, China). Fluorescence spectrophotometer (Shimadzu RF-5301, PL, Shimadzu Corporation of Japan, kyoto, Japan) was used to analyze the photoelectron–hole recombination rate of the samples. The excitation wavelength was 325 nm. The photocatalytic effect of the materials was measured by uV-757 CRT, and $BaSO_4$ was used as reflection reference substance.

2.4. Photocatalytic Performance Test

The photocatalytic effect of simulated organic dye wastewater (20 mg/L rhodamine B (RhB)) was evaluated at room temperature. A 300 W xenon lamp (GX2500, Shanghai Jiguang Special Lighting Electric Appliance Factory, Shanghai, China) was used as a simulated solar light to test the light catalytic performance of the prepared samples. Take 50 mL RhB into a beaker and add 50 mg photocatalytic material. Firstly, the beaker was stirred for 1 h under no light to achieve the dynamic equilibrium of adsorption–desorption on the surface of the composite material. Then, 6 mL of the mixed solution was placed in a centrifugal tube. After 10 min of centrifugation, the supernatant was taken and placed in a quartz colorimetric dish. The initial absorbance was measured and marked as A0. Turn on the simulated light for irradiation, then take out 4 mL of the mixed solution every 30 min and repeat the above steps. Take the supernatant and place it in a quartz coloration to measure the absorbance of the dye (A1, A2, A3⋯).

2.5. Electrochemical Measurement

Electrochemical impedance spectroscopy (EIS) was carried out on a VMP3 workstation, as was Mott–Schottky. The workstation is equipped with three electrodes, including glassy carbon, platinum, and saturated calomel. The preparation method of the working electrode was as follows: 2 mg sample was placed in a small sample tube, 200 μL ethanol reagent

was added, and ultrasonic dispersion for 1 h. The above sample suspension is moved with a suction gun and laid on the conductive layer of the glassy carbon electrode, and it can be dried. During the experiment, Na_2SO_4 (0.5 M) was used as electrolyte solution. EIS was tested in the range of 0.01 kHz to1 kHz. Motshottky (MS) plots were measured at 1 kHz and the voltage was −1–1 v.

3. Results and Discussion

3.1. XRD Analysis

Figure 3 illustrates the X-ray diffraction patterns for the CeO_2 prepared at different temperatures and UiO-66-NH_2 substance. It can be observed that the diffraction peak of the CeO_2 samples prepared at different temperatures are consistent with the standard card (JCPDS 34-0394) peak. The characteristic peaks at 2θ = 28.55°, 33.08°, 47.48°, 56.33°, 59.09°, 69.4°, 76.7°, and 79.07° correspond to (111), (200), (220), (311), (222), (400), (311) and (420) of cubic phase CeO_2, respectively. This indicates that CeO_2 synthesized in this paper is a cube structure and its space group is Fm-3m (225). Moreover, it can also be displayed from Figure 3 that the X-ray diffraction peaks of the UiO-66-NH_2 made are the same as those of literature and simulation [29,30], explaining that the UiO-66-NH_2 material has been synthesized in this paper. Figure 4 states the XRD peaks of 1-Ce/UN at different temperatures. It can be observed that the characteristic peak of cubic CeO_2 is the strongest at 400 °C with the increase of temperature, and the phase crystallization is the best at this temperature. Figure 5 is XRD patterns of 400 °C Ce/UN with different composite proportions. Referring to Figures 4 and 5, the XRD peaks of Ce/UN with diverse proportions and different temperatures are consistent with the representative peaks of UiO-66-NH_2 and CeO_2. No other XRD peaks were found due to any impurities, indicating the high purity of the composite. The major diffraction peaks of the composites at 7.3° and 8.4° correspond to the typical peak of UiO-66-NH_2, and the pattern is maintained well. The diffraction reflections at 28.55°, 33.08°, 47.48°, and 56.33° are related to (111), (200), (220), and (311) crystal planes of CeO_2, which clearly indicates the phase formation of Ce/UN nanocomposites. The strong and sharp diffraction peaks indicate that Ce/UN nanocomposites have good crystallinity.

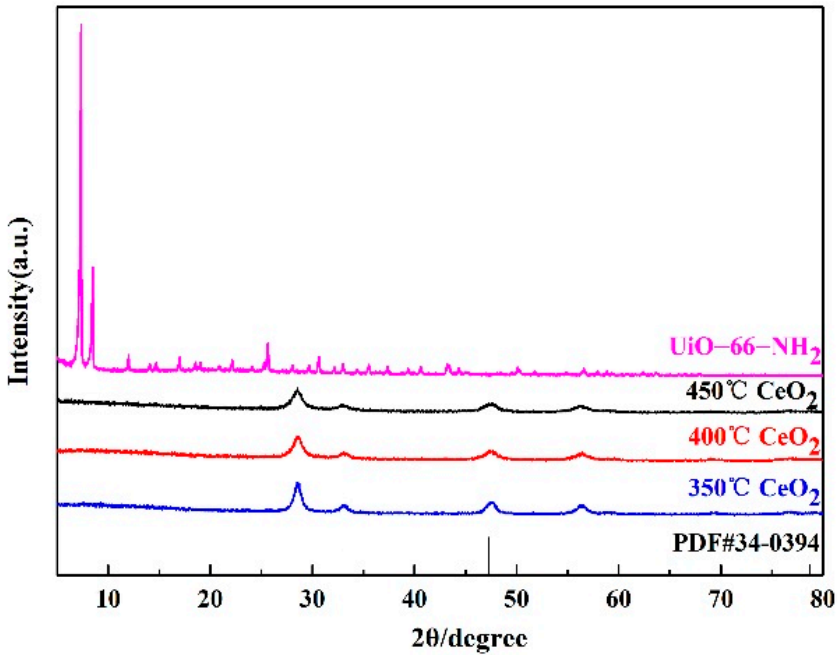

Figure 3. XRD patterns of CeO_2 prepared at different temperatures and UiO-66-NH_2.

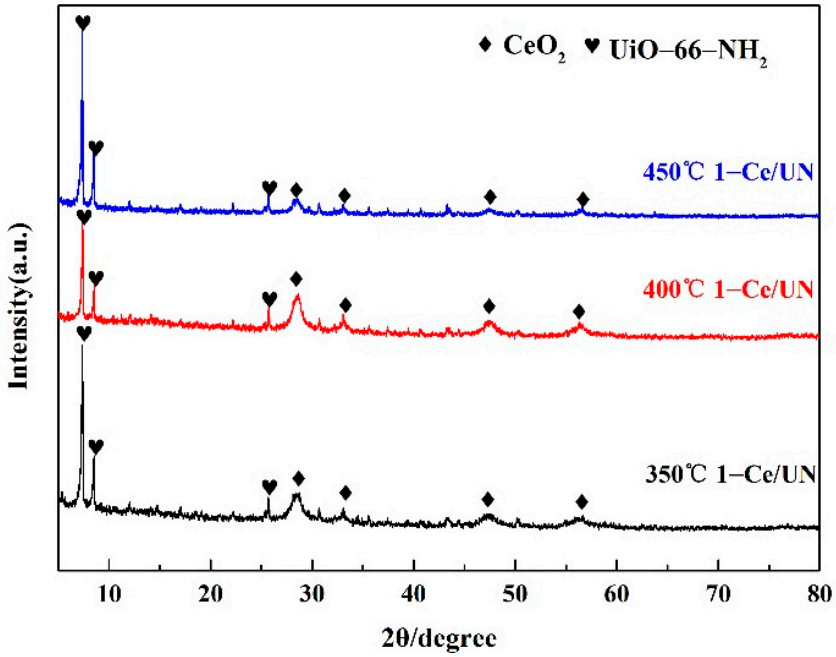

Figure 4. XRD patterns of 1-Ce/UN at different temperatures.

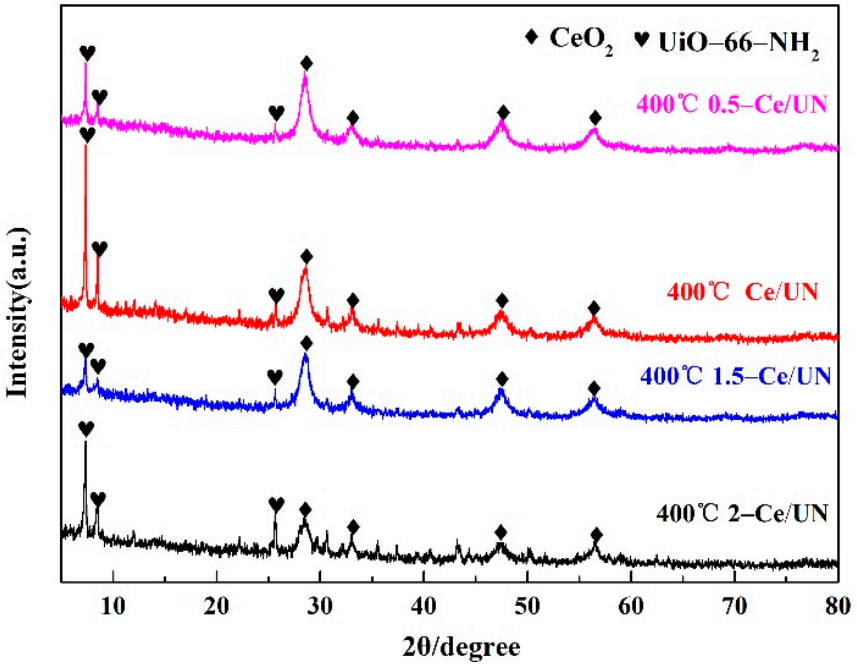

Figure 5. XRD patterns of 400 °C Ce/UN with different composite proportions.

3.2. SEM Analysis

The microtopography of CeO_2 calcined at different temperatures and UiO-66-NH_2 were analyzed by SEM, as shown in Figure 6. According to Figure 6a–c, the CeO_2 calcined at different temperatures all present a 3D flower-like structure. The length of CeO_2 sheet is about 5 μm, and the width is about 2 μm (as shown in Figure 6a). In addition, the nanosheets gradually increase in size with increasing temperature, which provides a large contact area for the transfer of $e^- - h^+$, and can be loaded on UiO-66-NH_2 well. From Figure 6d, it can be observed that the UiO-66-NH_2 is a particle with a regular octahedral structure. Its average size is about 200–500 nm.

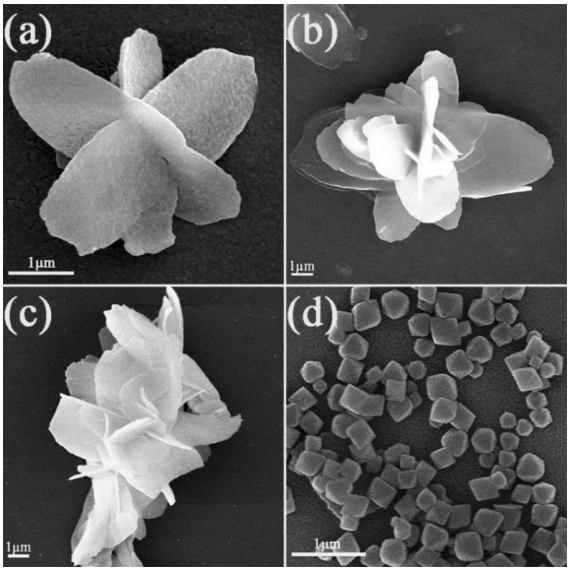

Figure 6. SEM images of (**a**) 350 °C CeO_2, (**b**) 400 °C CeO_2, (**c**) 450 °C CeO_2, and (**d**) UiO-66-NH_2.

Figure 7 shows the microstructure of CeO_2 calcined at different temperatures and UiO-66-NH_2 composites in the 1:1 ratio. It is not difficult to find that particles of UiO-66-NH_2 are covered on pure CeO_2 nanosheets, and the diameter of UiO-66-NH_2 is about 200–500 nm. During sample preparation, ultrasonic treatment does not separate UiO-66-NH_2 from CeO_2, instructing that UiO-66-NH_2 is well attached to CeO_2. The interface formed between ions may have good interaction. Figure 8 shows the morphologies of CeO_2 (calcined at 400 °C) and UiO-66-NH_2 composites in different proportions. It can be observed that the agglomeration of UiO-66-NH_2 nanoparticles on CeO_2 flower nanosheets decreases with the decrease of the content of UiO-66-NH_2. When the ratio of CeO_2 to UiO-66-NH_2 is 1:1, the Ce/UN composites have the best photocatalytic properties of all substances (This will be studied in detail in the photocatalytic experimental section), so the focus of detailed study is on 400 °C 1-Ce/UN. Figure 9 presents the element mapping analysis on the 400 °C 1-Ce/UN composites. It can be seen that the elements of Ce, O (specific elements of CeO_2), Zr and N (representative element of UiO-66-NH_2) appear in the Ce/UN composites and are evenly distributed. Table 1 shows the SEM-EDS analysis of area "a" signed in Figure 9a. The results show that the analyzed region may contain CeO_2 and UiO-66-NH_2. Combined with the XRD test results (Figures 4 and 5), it can be further inferred that the Ce/UN composite materials were synthesized.

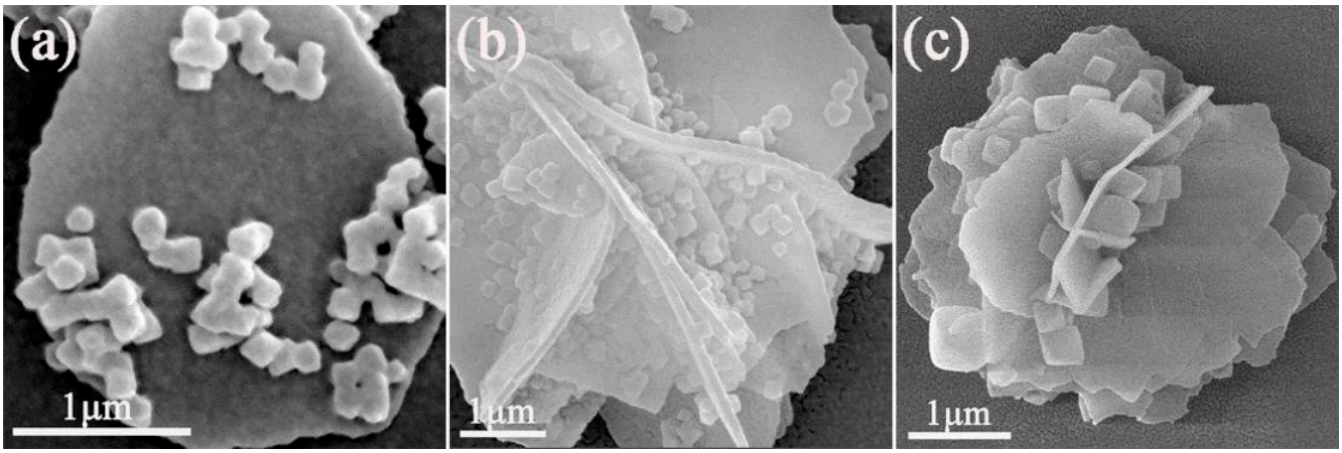

Figure 7. SEM morphologies of Ce/UN composites: (**a**) 350 °C 1-Ce/UN; (**b**) 400 °C 1-Ce/UN; (**c**) 450 °C 1-Ce/UN.

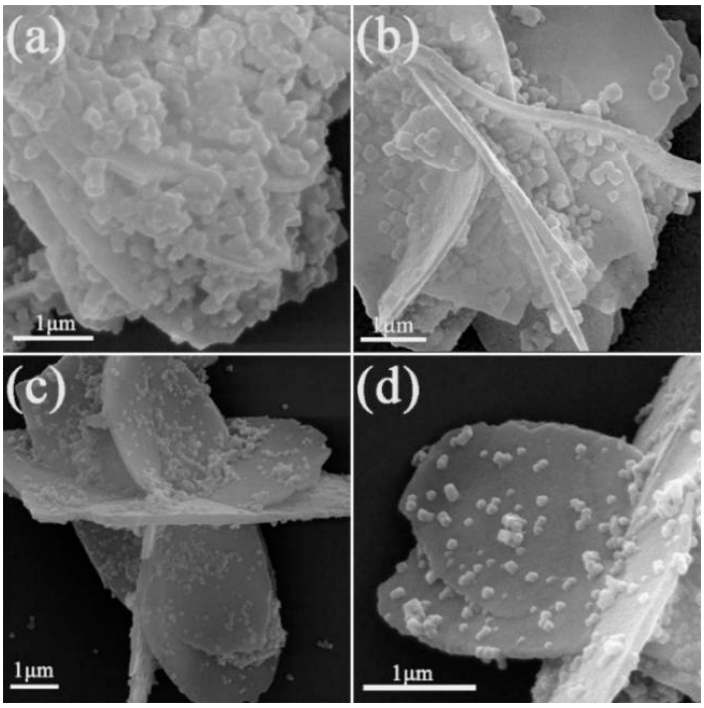

Figure 8. SEM morphologies of Ce/UN composites with different proportions: (**a**) 0.5:1; (**b**) 1:1; (**c**) 1.5:1; (**d**) 2:1.

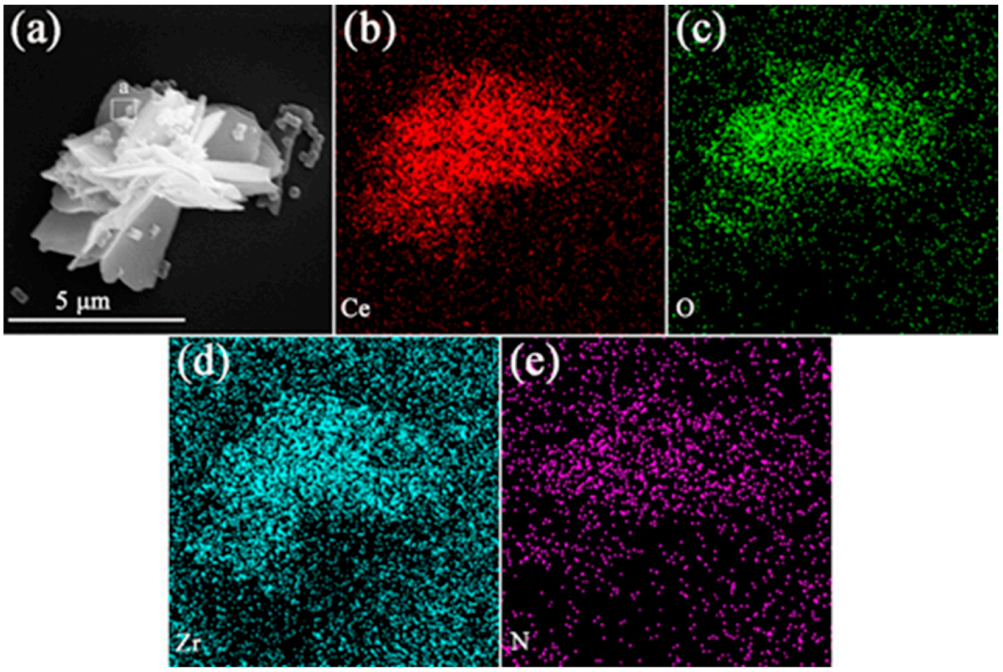

Figure 9. Elements maps analysis of 400 °C 1-Ce/UN composites: (**a**) SEM image; (**b**–**e**) element analysis of Ce, O, Zr and N.

Table 1. The EDS results of the area "a" signed in Figure 9a.

Position	Composition (wt. %)				Possible Phases
	Ce	O	Zr	N	
a	76.2	24.5	3.23	0.91	CeO_2, UiO-66-NH_2

3.3. TEM Analysis

The shape and interfacial structures of CeO_2, UiO-66-NH_2, and 400 °C 1-Ce/UN were analyzed by TEM and HRTEM, as shown in Figure 10. According to Figure 10a, the lattice fringe spacing of CeO_2 is about 0.196 nm, which is well matched with the (220) crystal plane. TEM images shown in Figure 10b indicate that UiO-66-NH_2 has an octahedral construction with a maximum length of about 300 nm. Figure 10c further demonstrates that UiO-66-NH_2 is finely scattered on the flower-like structure of CeO_2. Octahedral UiO-66-NH_2 with a surface diameter of about 300 nm is in close contact with flower-like CeO_2, which matches the XRD results. In addition, according to the Figure 10d, the interface between CeO_2 and UiO-66-NH_2 can be clearly observed (shown as the white dotted line in Figure 10d), confirming the composition of heterostructures between them. These results suggest that UiO-66-NH_2 was successfully grown on CeO_2 flower nanosheets and interlinked, which may contribute to the segregation of photogenerated carriers.

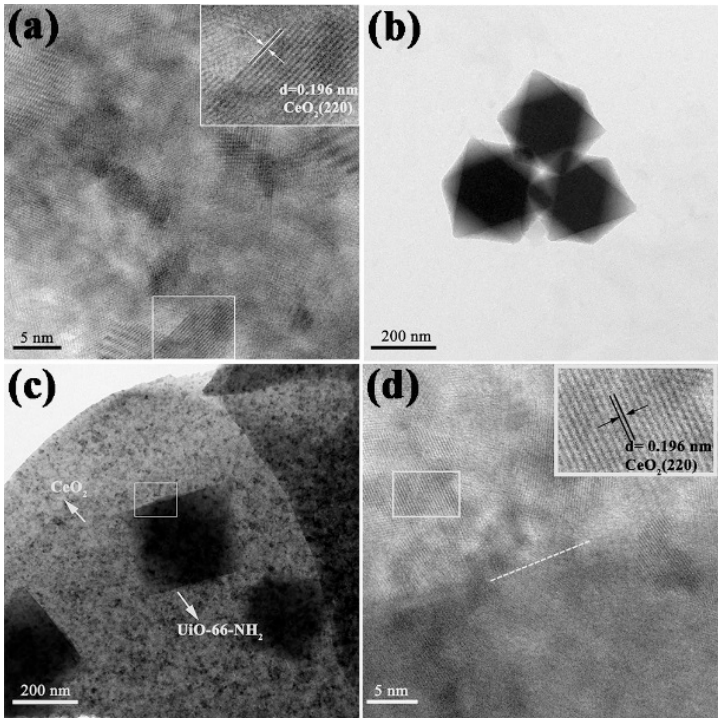

Figure 10. TEM and HRTEM images of samples: (**a**) CeO_2; (**b**) UiO-66-NH_2; (**c**) 400 °C 1-Ce/UN composites; (**d**) magnified HRTEM image of the white box labelled in (**c**).

3.4. XPS Analysis

The chemical states and bonding environment of 400 °C 1-Ce/UN were studied by XPS analysis. The results are shown in Figure 11. The total measurement spectrum (Figure 11a) confirmed that Ce/UN heterostructure composite contained Ce, O, Zr, and N elements, which was consistent with the element distribution diagram of SEM-EDS (Figure 9). For the high-resolution spectrum of Ce 3d, the 883.4 eV, 889.6 eV, and 899.3 eV characteristic peaks shown in Figure 11b are attributed to the binding energy of Ce $3d_{5/2}$. In addition, these three peak-to-peak values are 901.9 eV, 907.8 eV, and 917.6 eV, respectively, which belong to the binding energy of Ce $3d_{1/2}$ [31,32]. In Figure 11c, the binding energies of Ze $3d_{5/2}$ and Zr $3d_{3/2}$ are about 182.4 eV and 184.7 eV, respectively [33]. This demonstrates the existence of Zr^{4+} in zirconium oxygen clusters. In addition, the O1s peak at 529.7 eV in Figure 11d belongs to the lattice oxygen in Ce-O bond and Zr-O bond [4,34].

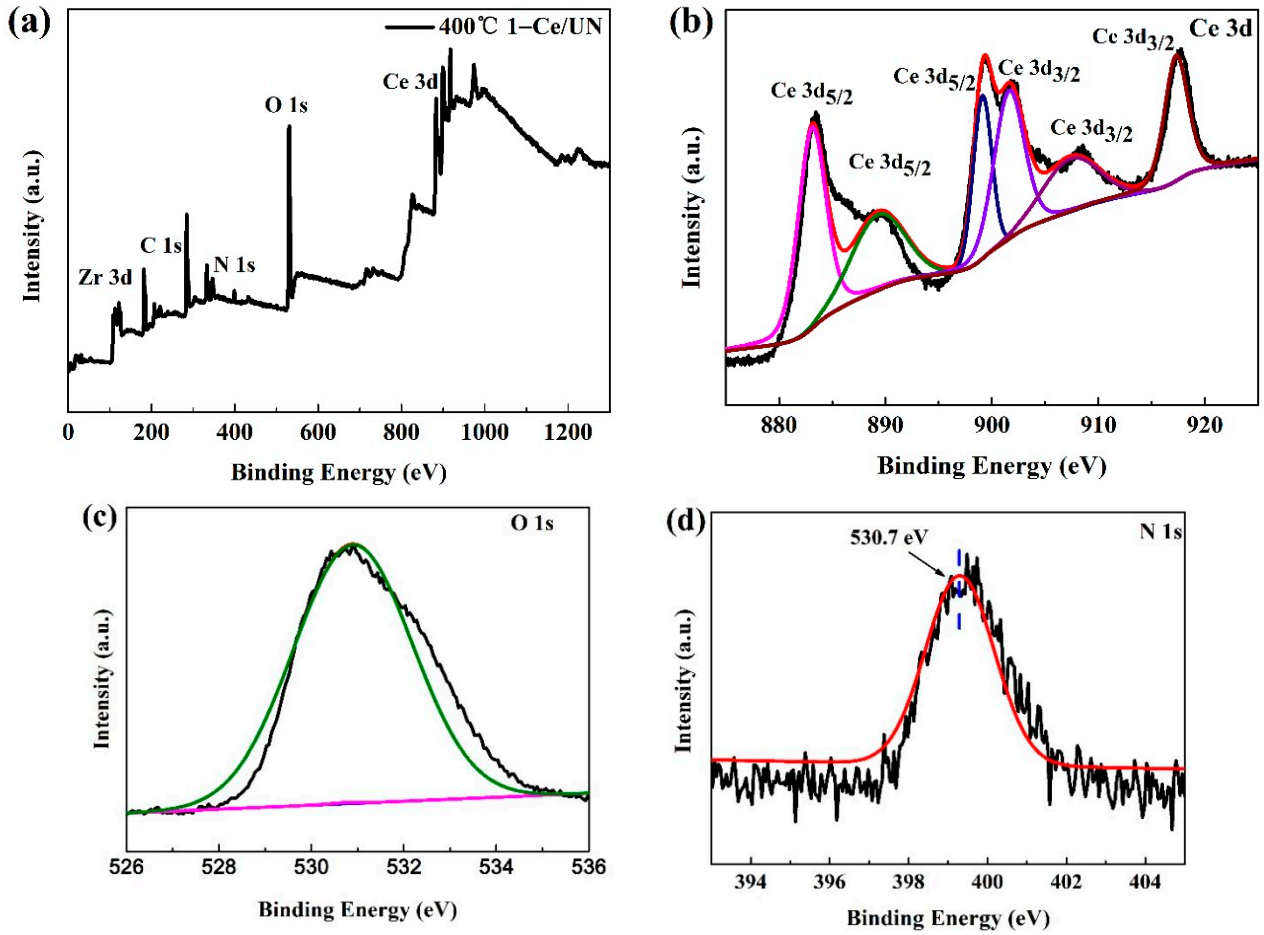

Figure 11. XPS spectra of 400 °C 1-Ce/UN catalyst: (**a**) Survey, (**b**) Ce3d, (**c**) O1s, (**d**) N1s.

3.5. BET Analysis

Figure 12a displays that the N_2 adsorption–desorption isotherm was applied to investigate the specific surface area and pore size distribution of synthetic materials. It could be found that the specific surface area of 400 °C 1-Ce/UN was higher than that of CeO_2 after introducing UiO-66-NH_2, indicating that UiO-66-NH_2 could significantly increase the specific surface area of the composites. As shown in Figure 12b, the values of BET surface area of UiO-66-NH_2 are 1331.0 m^2/g, and UiO-66-NH_2 displayed a typical type IV isotherm with a H3-shaped hysteresis loop observed in the range 0.6–1.0 P/P_0, indicating its mesoporous structure based on the IUPAC classification. In addition, the pore size distribution confirmed that the pores in UiO-66-NH_2 were 3.9 nm, which mainly distributed in the range 2–50 nm, corresponding to a mesoporous structure. According to Figure 12c, the specific surface areas of CeO_2 were 326.4 m^2/g and the pore size was 4.2 nm. The pore size distribution results showed that CeO_2 is mesoporous. Among the composites, the BET specific surface area of 400 °C 1-Ce/UN is 613.9 m^2/g, and the pore size is 4.0 nm (as shown in Figure 12d). Although the specific surface area of 400 °C 1-Ce/UN is lower than that of UiO-66-NH_2, it is much higher than CeO_2, demonstrating that 400 °C 1-Ce/UN heterojunction can provide abundant surface active sites and facilitate photoexcited charge carriers transfer [35].

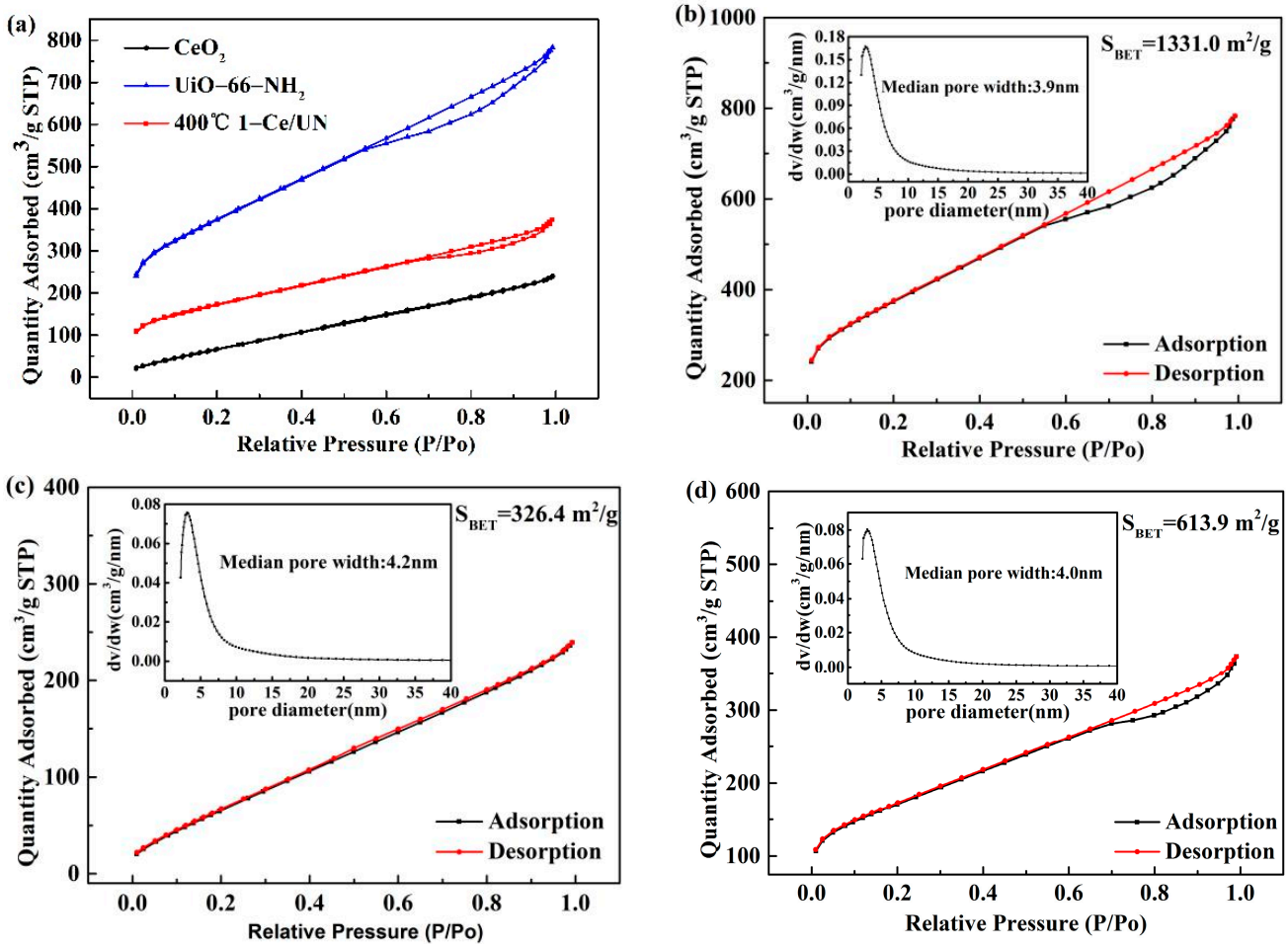

Figure 12. (**a**) N_2 adsorption–desorption isotherms of CeO_2, UiO-66-NH_2 and 400 °C 1-Ce/UN; (**b**) N_2 adsorption–desorption isotherms and the pore size distribution of UiO-66-NH_2; (**c**) N_2 adsorption–desorption isotherms and the pore size distribution of CeO_2; (**d**) N_2 adsorption–desorption isotherms and the pore size distribution of 400 °C 1-Ce/UN.

3.6. Optical Properties

The characteristics of absorption in optics and band gap of CeO_2, UiO-66-NH_2 and Ce/UN were studied by using UV-vis DRS, and then the visible light utilization rate of the composites was analyzed, as shown in Figure 13. According to Figure 13a, the light absorption values of CeO_2 are about 430 nm, respectively, which are in good agreement with the results of previous studies [36,37]. In addition, according to Figure 13a,b, compared with CeO_2, 400 °C 1-Ce/UN showed a longer wavelength absorption edge. In addition, the edge of the absorption peak is about 440 nm. Therefore, introducing UiO-66-NH_2 into CeO_2 can boost its own light utilization property, and the Ce/UN heterojunction makes the absorption edge of the material move to the right, resulting in a larger absorption wavelength, so that it can absorb more visible light.

The visible light absorption performance of Ce/UN heterojunction shows that it can be a good visible- light absorption semiconductor material. Typically, the band gap (Eg) of the photocatalyst can be obtained from Kubelke–Munk equation $(\alpha hv) = A(hv - Eg)^n$, where α is the absorption with respect to the optics coefficient and H is the energy with respect to photons. Since CeO_2 is an immediate transition band gap, and UiO-66-NH_2 is an indirect transition Eg, and the n value is 1/2 and 2 in this study. By plotting $(hv - Eg)^2$ and $(hv - Eg)^{1/2}$, the band gap can be determined by the tangent intercept. According to Figure 13a,c, the bandgap widths of CeO_2 and UiO-66-NH_2 are about 2.86 eV and 2.65 eV apart. Flat band potential (U_{fb}) and semiconductor types were calculated using

Mott–Schottky (MS) plots. According to Figure 13d,e, under the condition of 1 kHz, CeO_2 and UiO-66-NH_2 are fitted with positive slopes, both of which are the semiconductors type that belongs to the n type. Furthermore, the U_{fb} of CeO_2 and UiO-66-NH_2 are −0.63 eV and −0.64 eV, respectively. In general, U_{fb} has 0.1 eV more potential than a conduction band (CB) for most N-type semiconductors [38]. Therefore, the ratio of the bottom CB of CeO_2 and the lowest unoccupied molecular orbital (LUMO) of UiO-66-NH_2 to NHE is −0.73 eV and −0.74 eV, respectively. Combine the Eg value of VIOLET UV-vis DRS and $Eg = E_{VB} - E_{CB}$. The HOMO ratio of CeO_2 and UiO-66-NH_2 to NHE is 2.13 eV and 1.91 eV, respectively.

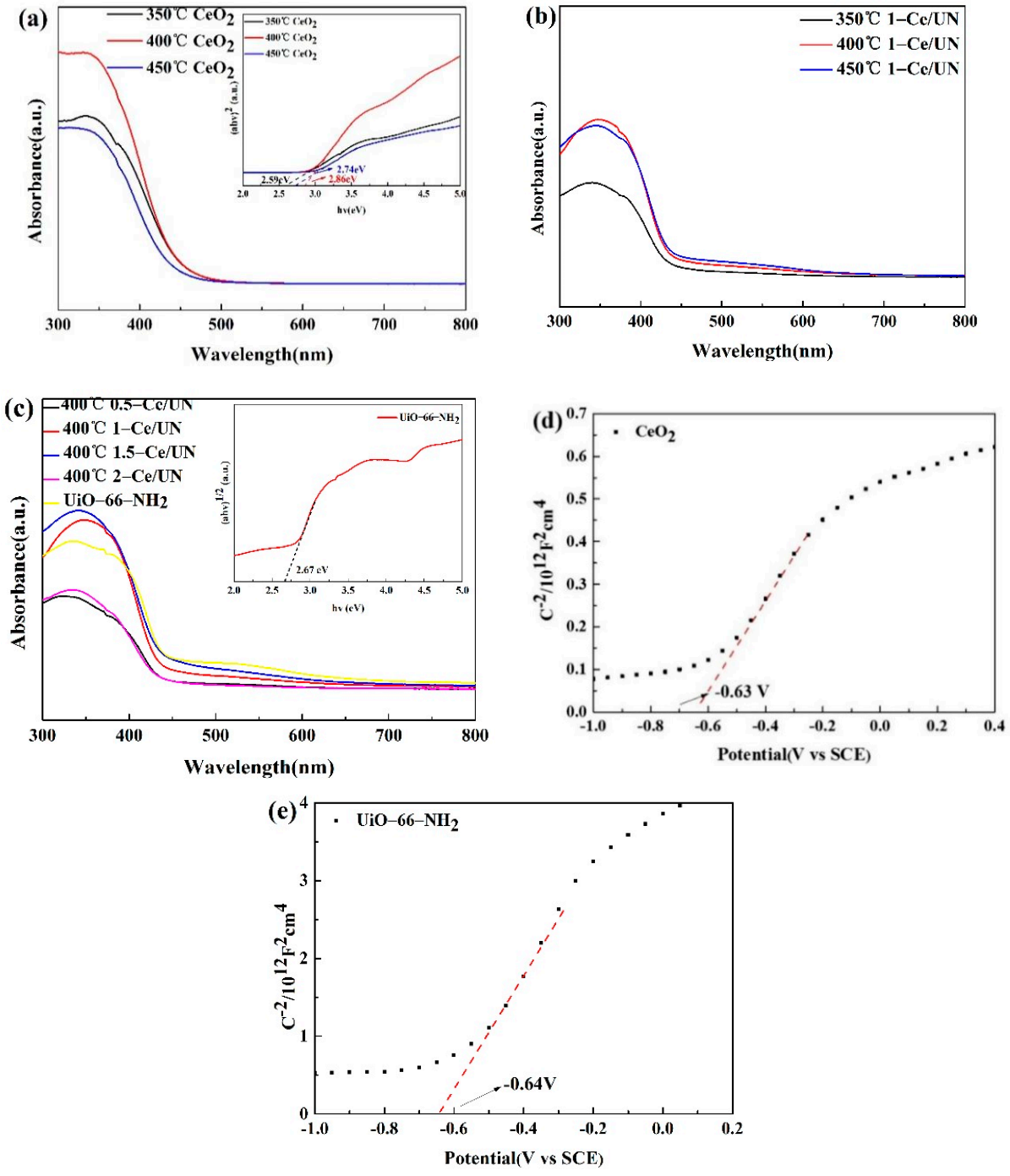

Figure 13. UV-Vis reflectance spectrum of (**a**) CeO_2 prepared at different temperatures, (**b**) (350 °C, 400 °C, 450 °C)1-Ce/UN, (**c**) Ce/UN composites with different composite ratios, and the Mott–Schottky curve of (**d**) CeO_2 and (**e**) UiO-66-NH_2.

3.7. Properties about Electrochemistry and the PL Emission Spectra

The mechanism of photocatalytic activity was studied by EIS and the PL emission spectra emission spectroscopy, and the results are shown in Figure 14. EIS study is required to confirm and elucidate its good photocatalytic performance. From Figure 14a, it can be observed that 400 °C 1-Ce/UN has a smaller arc size than pure matter. Usually, according to EIS images, semi-arcs can reflect the recharge course because the size of it is related to the resistance. In addition, smaller arcs reflect smaller charge transfer resistance [39]. Therefore, EIS results show that the charge separation rate of 400 °C 1-Ce/UN is higher and the charge transfer rate is faster because of the lead-in of UiO-66-NH_2. The results of EIS show that photocarrier separation of 400 °C 1-Ce/UN may be due to the formation of the heterojunction.

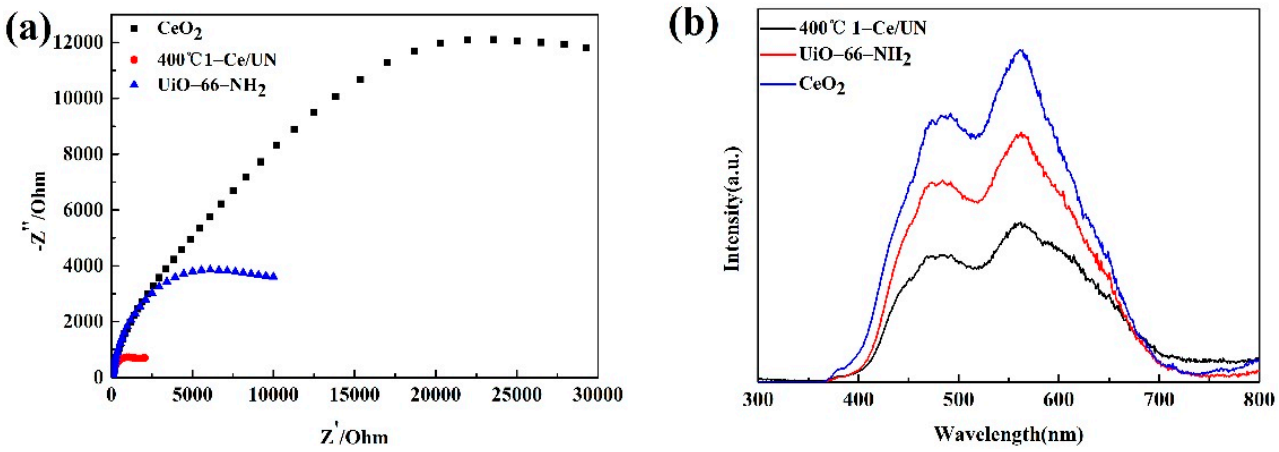

Figure 14. CeO_2, UiO-66-NH_2 and 400 °C 1-Ce/UN (**a**) EIS Nyquist diagram and (**b**) PL diagram.

The photoluminescence (PL) emission spectrum further demonstrated the photoluminescence separation of electron–hole pairs at 400 °C 1-Ce/UN. According to Figure 14b, it can be found that the luminescence peaks of CeO_2 and UiO-66-NH_2 appear at about 470 nm and 570 nm, separately. The emission peak at about 470 nm may be a combination of electron hole radiation between CB and valence band (VB), and the emission peak at about 570 nm may be consistent with the good state emission [40]. In general, weak fluorescence intensity means a high photoinduced electron–hole pair separation rate, which can effectively restain the electron–hole for restructuring, and effective photocarrier separation can prolong the service life of photocatalyst, improve interfacial charge shift efficiency, and boost the photocatalytic efficiency [41]. The luminescence intensity of 400 °C 1-Ce/UN composite is obviously weaker than the pure substance, indicating that the electron and hole separation rate of 400 °C 1-Ce/UN can be effectively inhibited. The peak intensity of 400 °C 1-Ce/UN is lower than that of pure substances, which boosted the interfacial electronic shift and also corresponds to the consequences of photocatalytic degradation. Therefore, Ce/UN has a good photocatalytic property, which is consistent with the EIS conclusion mentioned above.

3.8. Photocatalytic Degradation Performance

The Photocatalytic property of 20 mg/L RhB was studied under simulated sunlight (room temperature) irradiation. The photocatalytic property of RhB was researched by comparing the photocatalytic property of RhB with the photocatalytic activity of RhB. The degradation rates of CeO_2, UiO-66-NH_2, Ce/UN at different temperatures, and Ce/UN at different proportions are studied. The results are shown in Figure 15. The catalyst is 10 mg in simulated wastewater. It can be seen from Figure 15a that the removal rates of RhB by CeO_2 and UiO-66-NH_2 alone reached 0% and 60% within 4 h, respectively. With the increase of CeO_2 temperature, the photocatalytic properties of the sample increased first and then decreased. Thus, the temperature of CeO_2 with the best degradation performance

was found to be 400 °C. For pure CeO_2, the adsorption efficiency was only 1% at the dark adsorption stage of 60 min. In addition, for UiO-66-NH_2, the rate of adsorption is only 52% after dark adsorption for 60 min. The photocatalytic performance of 400 °C 1-Ce/UN composite in a dark adsorption stage is better than that of pure substances, and the adsorption efficiency reaches 60%. Because of the three-dimensional porous structure of UiO-66-NH_2, the adsorption property of RhB is stronger. Thus, the rate of degradation of 400 °C 1-Ce/UN can reach 96%. The high degradation efficiency indicates that the combination of two-dimensional CeO_2 flower nanosheets with UiO-66-NH_2 has good oxidation capacity.

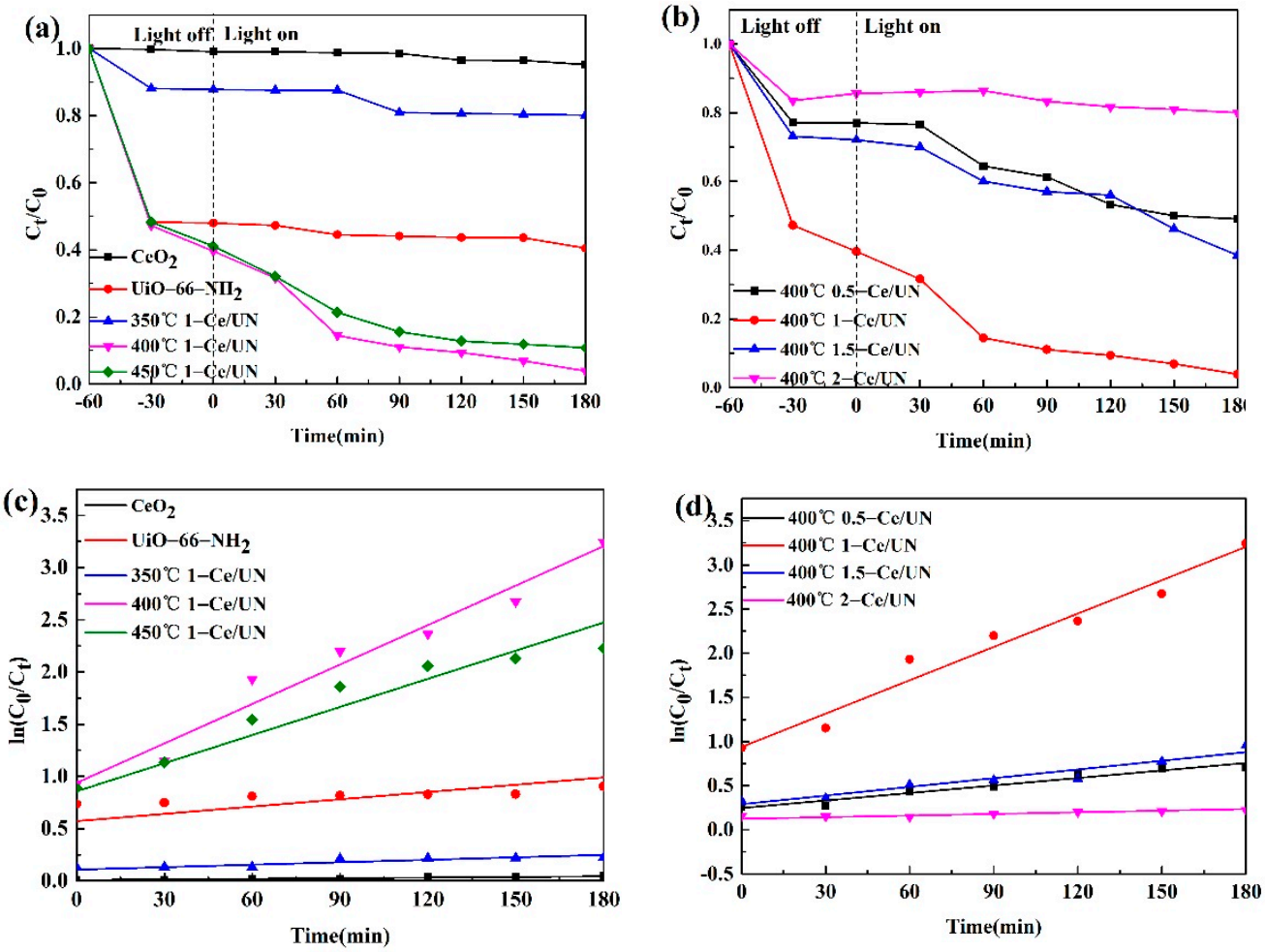

Figure 15. Degradation rate and first-order kinetic K diagram of RhB by CeO_2, UiO-66-NH_2, and Ce/UN: (**a**) degradation rate of different temperatures; (**b**) degradation rate of different proportions; (**c**) first-order kinetic K-value diagram of different temperatures; (**d**) first-order kinetic K-value diagram of different proportions.

Compared with pure CeO_2, the adsorption performance of Ce/UN is improved, so that the composite can effectively degrade pollutants. As shown in Figure 15b, the photocatalytic effect changes significantly after the two catalysts were combined, and with the increase of the CeO_2 ratio, the photocatalyst properties of the composites increased first and then decreased. Thus, the photocatalytic efficiency can be improved. This phenomenon indicates that the structure of heterojunction is very favorable to photocatalytic degradation under certain conditions. The proper combination of UiO-66-NH_2 is a vital reason to determine the photocatalytic property of UiO-66-NH_2, and an excessive or insufficient reaction rate will decrease. It may be because of the obvious agglomeration of UiO-66-NH_2 on the surface of CeO_2 flower nanosheets. This may lead to accelerated

charge recombination, which in turn inhibits carrier separation [42]. Meanwhile, the negative effects of excessive UiO-66-NH_2 may be because of the shielding and blocking effects of active sites [43]. Therefore, the best photocatalytic activity of the composite when the suitable quality of UiO-66-NH_2 is added.

The aim is to further study the degradation process of RhB by a photocatalyst; the Langmuir-Hinshelwood (L-H) model $-\ln\left(\frac{C_t}{C_0}\right) = kt$ was used to fit the reaction kinetics curve, in which K was the speed constant (min^{-1}), C_0 is the initial concentration of RhB (mol/L), and C_t is the concentration of RhB at time T (mol/L). According to Figure 15c, under the conditions of pure CeO_2, UiO-66-NH_2, 350 °C 1-Ce/UN, 400 °C 1-Ce/UN, and 450 °C 1-Ce/UN, the estimated rate constants K are 0.0002, 0.0023, 0.0008, 0.0126, and 0.0089, respectively. According to Figure 15d, under the conditions of 400 °C 0.5-Ce/UN, 400 °C 1-Ce/UN, 400 °C 1.5-Ce/UN and 400 °C 2-Ce/UN, the estimated rate constants k are 0.0028, 0.0126, 0.0033, and 0.0006, respectively. The results show that 400 °C 1-Ce/UN has a high rate constant, which is 20 times the pure CeO_2 and 1.6 times the UiO-66-NH_2, respectively. When CeO_2 temperature is too high or the composite amount is too much, the photocatalytic activity of the composite material will be reduced, and the carrier in the composite material will be reduced. The low charge transfer rate and the accelerated reassociation of electron holes lead to the decrease of photocatalytic properties of the materials.

3.9. Photocatalytic Mechanism

By introducing 0.1 mM free radicals of $Na_2C_2O_4$ (holes$^+$ scavenger), isopropyl alcohol (IPA, •OH scavenger), and p-benzoquinone (BQ, $\cdot O_2^-$ scavenger), active material involved in the degradation related to photocatalysis was investigated, and the possible mechanism made was discussed, as shown in Figure 16. After 400 °C 1-Ce/UN, the degradation rate of RhB decreased to 96% within 4 h. After the addition of $Na_2C_2O_4$, the photocatalytic degradation rate decreases, which can be concluded as (Equations (1)–(3)). The presence of $Na_2C_2O_4$ significantly reduces the photocatalytic RhB degradation efficiency, indicating that the consumed holes are not conducive to the separation of $e^- - h^+$. With the BQ coming in, the degradation efficiency of RhB also obviously declined. Therefore, it can be seen that H^+ and $\cdot O_2^-$ are the main species responsible for the degradation of RhB rather than •OH. In a degradation reaction, the •OH effect is relatively small:

$$CeO_2/UiO - 66 - NH_2 + hv \rightarrow h^+ + e^- \quad (1)$$

$$e^- + O_2 \rightarrow \cdot O_2^- \quad (2)$$

$$O_2^- + h^+ + RhB \rightarrow Products \quad (3)$$

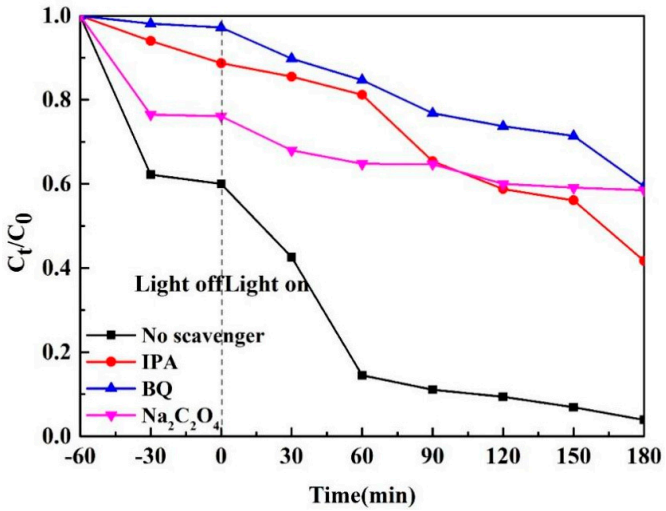

Figure 16. Effect of different scavenger on photocatalytic degradation of RhB by 400 °C 1−Ce/UN.

According to the obtained results, the mechanism of Ce/UN composite made in photocatalysis was analyzed in depth (as shown in Figure 17). Both CeO_2 and UiO-66-NH_2 can generate $e^- - h^+$ upon visible light. Because of the potential difference between the CB of UiO-66-NH_2 and CB of CeO_2 at −0.74 eV, the light-generated electrons are transferred from the CB of CeO_2 to CB of UiO-66-NH_2. Both the LUMO of CeO_2 and UiO-66-NH_2 generate O_2^- because their potential is higher than O_2/O_2^- (−0.33 eV vs. NHE) [44].

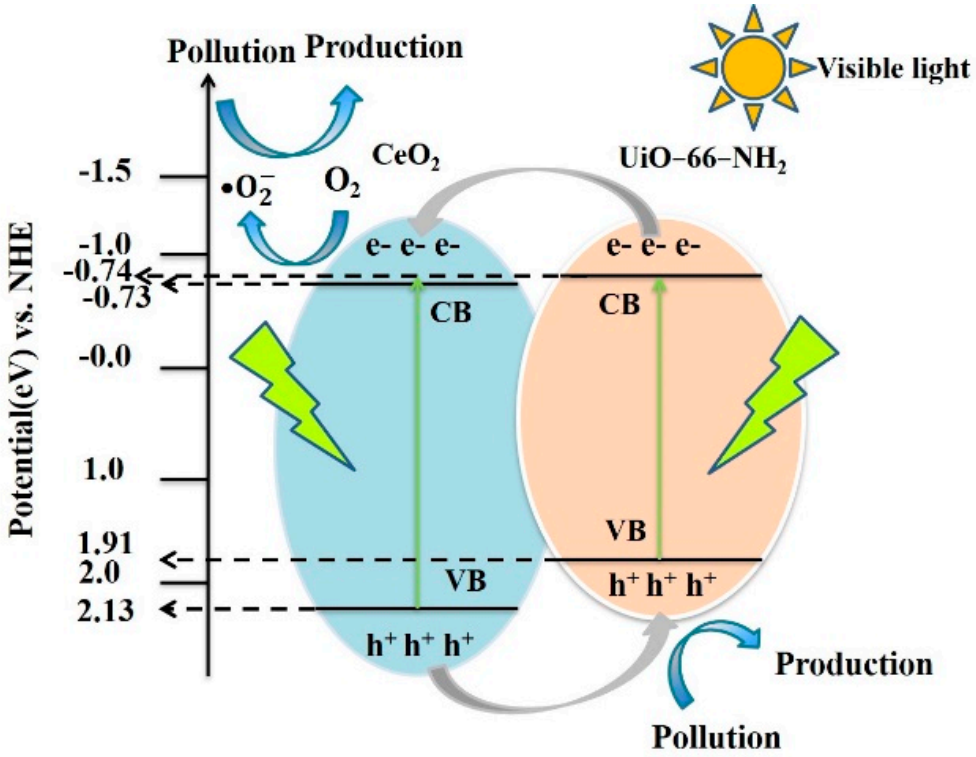

Figure 17. Photocatalytic mechanism of a Ce/UN composite.

4. Conclusions

In this paper, a Ce/UN composite photocatalyst was in-situ synthesized by a hydrothermal method. The photocatalytic properties and degradation mechanism of composites were studied in detail. The results show that the Ce/UN composite photocatalyst shows better degradation efficiency of RhB than CeO_2 and UiO-66-NH_2 under the situation of simulated sunlight. The degradation rate of RhB reached about 96% after 4 h photocatalysis, which is much higher than CeO_2 (4.5%) and UiO-66-NH_2 (54%) under the same conditions. The enhancement of the photocatalytic performance of the Ce/UN may be because of the formation of heterojunction. It can be observed that Ce/UN composites present a 3D flower-like structure, and UiO-66-NH_2 particles are covered on CeO_2 nanosheets. This heterojunction structure may provide a large contact area for the transfer of $e^- - h^+$. In addition, a Ce/UN composite photocatalyst has lower charge transfer resistance and luminescence intensity compared with two pure substances according to the results of EIS and PL, which is beneficial to the separation of photocarriers and the improvement of the interfacial charge transfer efficiency. The free radical capture experiments show that H^+ and $\cdot O_2^-$ are the main active species in the photocatalytic process.

Author Contributions: Writing-Original draft preparation, Z.L.; Reviewing and Editing, Y.Z.; Funding acquisition, Y.Z.; Project Administration, L.D.; Resources, L.D.; Formal analysis, L.D.; Reviewing and Editing, H.M.; Formal analysis, H.M.; Validation, S.T.; Data curation, S.T.; Data curation, L.W.; Investigation, A.H. All authors have read and agreed to the published version of the manuscript.

Funding: This research received no external funding.

Institutional Review Board Statement: Not applicable.

Informed Consent Statement: Not applicable.

Data Availability Statement: The data presented in this study are available on request from the corresponding author.

Acknowledgments: This research was supported by the National Natural Science Foundation of China (NSFC, 52105332), the General Program of State Key Laboratory of Advanced Welding and Joining (AWJ-22M15), and the Open Foundation Guangxi Key Laboratory of Optical and Electronic Materials and Devices (20KF14).

Conflicts of Interest: The authors declare no conflict of interest.

References

1. Ajmal, A.; Majeed, I.; Malik, R.N.; Idriss, H.; Nadeem, M.A. Principles and mechanisms of photocatalytic dye degradation on TiO_2 based photocatalysts: A comparative overview. *RSC Adv.* **2014**, *4*, 37003–37026. [CrossRef]
2. Gu, S.; Chen, Y.; Yuan, X.; Wang, H.; Chen, X.; Liu, Y.; Jiang, Q.; Wu, Z.; Zeng, G. Facile synthesis of CeO_2 nanoparticle sensitized CdS nanorod photocatalyst with improved visible-light photocatalytic degradation of rhodamine B. *RSC Adv.* **2015**, *5*, 79556–79564. [CrossRef]
3. Zheng, Y.; Liu, Y.; Guo, X.; Chen, Z.; Zhang, W.; Wang, Y.; Tang, X.; Zhang, Y.; Zhao, Y. Sulfur-doped g-C_3N_4/rGO porous nanosheets for highly efficient photocatalytic degradation of refractory contaminants. *J. Mater. Sci. Technol.* **2020**, *41*, 117–126. [CrossRef]
4. Wen, X.-J.; Niu, C.-G.; Zhang, L.; Liang, C.; Guo, H.; Zeng, G.-M. Photocatalytic degradation of ciprofloxacin by a novel Z-scheme CeO_2–Ag/AgBr photocatalyst: Influencing factors, possible degradation pathways, and mechanism insight. *J. Catal.* **2018**, *358*, 141–154. [CrossRef]
5. Wang, H.; Liao, B.; Lu, T.; Ai, Y.; Liu, G. Enhanced visible-light photocatalytic degradation of tetracycline by a novel hollow BiOCl@CeO_2 heterostructured microspheres: Structural characterization and reaction mechanism. *J. Hazard. Mater.* **2020**, *385*, 121552. [CrossRef]
6. Hu, S.; Zhou, F.; Wang, L.; Zhang, J. Preparation of Cu_2O/CeO_2 heterojunction photocatalyst for the degradation of Acid Orange 7 under visible light irradiation. *Catal. Commun.* **2011**, *12*, 794–797. [CrossRef]
7. Ma, R.; Zhang, S.; Wen, T.; Gu, P.; Li, L.; Zhao, G.; Niu, F.; Huang, Q.; Tang, Z.; Wang, X. A critical review on visible-light-response CeO_2-based photocatalysts with enhanced photooxidation of organic pollutants. *Catal. Today* **2019**, *335*, 20–30. [CrossRef]
8. He, J.; Zhou, L.; Liu, J.; Ling, Z.; Yang, L.; Zou, L.; Xiang, J.; Dong, S.; Yang, X. Modulation of surface structure and catalytic properties of cerium oxide nanoparticles by thermal and microwave synthesis techniques. *Appl. Surf. Sci.* **2017**, *402*, 469–477. [CrossRef]
9. Mansingh, S.; Padhi, D.K.; Parida, K.M. Enhanced visible light harnessing and oxygen vacancy promoted N, S co-doped CeO_2 nanoparticle: A challenging photocatalyst for Cr(vi) reduction. *Catal. Sci. Technol.* **2017**, *7*, 2772–2781. [CrossRef]
10. Xie, S.L.; Wang, Z.L.; Cheng, F.L.; Zhang, P.; Mai, W.J.; Tong, Y.X. Ceria and ceria-based nanostructured materials for photoenergy applications. *Nano Energy* **2017**, *34*, 313–337. [CrossRef]
11. Wu, B.; Shan, C.; Zhang, X.; Zhao, H.Y.; Ma, S.M.; Shi, Y.X.; Yang, J.; Bai, H.C.; Liu, Q. CeO_2/Co_3O_4 porous nanosheet prepared using rose petal as biotemplate for photo-catalytic degradation of organic contaminants. *Appl. Surf. Sci.* **2021**, *543*, 148677. [CrossRef]
12. Shen, C.-H.; Wen, X.-J.; Fei, Z.-H.; Liu, Z.-T.; Mu, Q.-M. Visible-light-driven activation of peroxymonosulfate for accelerating ciprofloxacin degradation using CeO_2/Co_3O_4 p-n heterojunction photocatalysts. *Chem. Eng. J.* **2020**, *391*, 123612. [CrossRef]
13. Pu, Y.; Luo, Y.; Wei, X.; Sun, J.; Li, L.; Zou, W.; Dong, L. Synergistic effects of Cu_2O-decorated CeO_2 on photocatalytic CO_2 reduction: Surface Lewis acid/base and oxygen defect. *Appl. Catal. B Environ.* **2019**, *254*, 580–586. [CrossRef]
14. Chae, B.W.; Amna, T.; Hassan, M.S.; Al-Deyab, S.S.; Khil, M.-S. CeO_2-Cu_2O composite nanofibers: Synthesis, characterization photocatalytic and electrochemical application. *Adv. Powder Technol.* **2017**, *28*, 230–235. [CrossRef]
15. You, D.; Pan, B.; Jiang, F.; Zhou, Y.; Su, W. CdS nanoparticles/CeO_2 nanorods composite with high-efficiency visible-light-driven photocatalytic activity. *Appl. Surf. Sci.* **2016**, *363*, 154–160. [CrossRef]
16. Lu, X.-H.; Xie, S.-L.; Zhai, T.; Zhao, Y.-F.; Zhang, P.; Zhang, Y.-L.; Tong, Y.-X. Monodisperse CeO_2/CdS heterostructured spheres: One-pot synthesis and enhanced photocatalytic hydrogen activity. *RSC Adv.* **2011**, *1*, 1207–1210. [CrossRef]
17. Zhang, P.; Liu, Y.; Tian, B.; Luo, Y.; Zhang, J. Synthesis of core-shell structured CdS@CeO_2 and CdS@TiO_2 composites and comparison of their photocatalytic activities for the selective oxidation of benzyl alcohol to benzaldehyde. *Catal. Today* **2017**, *281*, 181–188. [CrossRef]
18. Yaghi, O.M.; O'Keeffe, M.; Ockwig, N.W.; Chae, H.K.; Eddaoudi, M.; Kim, J. Reticular synthesis and the design of new materials. *Nature* **2003**, *423*, 705–714. [CrossRef]

19. Hasegawa, S.; Horike, S.; Matsuda, R.; Furukawa, S.; Mochizuki, K.; Kinoshita, Y.; Kitagawa, S. Three-Dimensional Porous Coordination Polymer Functionalized with Amide Groups Based on Tridentate Ligand: Selective Sorption and Catalysis. *J. Am. Chem. Soc.* **2007**, *129*, 2607–2614. [CrossRef]
20. Eddaoudi, M.; Kim, J.; Rosi, N.; Vodak, D.; Wachter, J.; O'Keeffe, M.; Yaghi, O.M. Systematic Design of Pore Size and Functionality in Isoreticular MOFs and Their Application in Methane Storage. *Science* **2002**, *295*, 469–472. [CrossRef]
21. Bibi, R.; Shen, Q.; Wei, L.F.; Hao, D.; Li, N.; Zhou, J. Hybrid BiOBr/UiO-66-NH2 composite with enhanced visible-light driven photocatalytic activity toward RhB dye degradation. *RSC Adv.* **2018**, *8*, 2048–2058. [CrossRef]
22. Sha, Z.; Wu, J. Enhanced visible-light photocatalytic performance of BiOBr/UiO-66(Zr) composite for dye degradation with the assistance of UiO-66. *RSC Adv.* **2015**, *5*, 39592–39600. [CrossRef]
23. Xu, X.-Y.; Chu, C.; Fu, H.; Du, X.-D.; Wang, P.; Zheng, W.; Wang, C.-C. Light-responsive UiO-66-NH_2/Ag_3PO_4 MOF-nanoparticle composites for the capture and release of sulfamethoxazole. *Chem. Eng. J.* **2018**, *350*, 436–444. [CrossRef]
24. Liang, Q.; Cui, S.; Liu, C.; Xu, S.; Yao, C.; Li, Z. Construction of CdS@UIO-66-NH_2 core-shell nanorods for enhanced photocatalytic activity with excellent photostability. *J. Colloid Interface Sci.* **2018**, *524*, 379–387. [CrossRef]
25. Wang, L.; Zheng, P.; Zhou, X.; Xu, M.; Liu, X. Facile fabrication of CdS/UiO-66-NH_2 heterojunction photocatalysts for efficient and stable photodegradation of pollution. *J. Photochem. Photobiol. A Chem.* **2019**, *376*, 80–87. [CrossRef]
26. Shen, L.; Liang, S.; Wu, W.; Liang, R.; Wu, L. CdS-decorated UiO–66(NH_2) nanocomposites fabricated by a facile photodeposition process: An efficient and stable visible-light-driven photocatalyst for selective oxidation of alcohols. *J. Mater. Chem. A* **2013**, *1*, 11473–11482. [CrossRef]
27. Jiang, D.; Fang, G.; Tong, Y.; Wu, X.; Wang, Y.; Hong, D.; Leng, W.; Liang, Z.; Tu, P.; Liu, L.; et al. Multifunctional Pd@UiO-66 Catalysts for Continuous Catalytic Upgrading of Ethanol to n-Butanol. *ACS Catal.* **2018**, *8*, 11973–11978. [CrossRef]
28. Ai, L.; Su, J.; Wang, M.; Jiang, J. Bamboo-Structured Nitrogen-Doped Carbon Nanotube Coencapsulating Cobalt and Molybdenum Carbide Nanoparticles: An Efficient Bifunctional Electrocatalyst for Overall Water Splitting. *ACS Sustain. Chem. Eng.* **2018**, *6*, 9912–9920. [CrossRef]
29. Katz, M.J.; Brown, Z.J.; Colón, Y.J.; Siu, P.W.; Scheidt, K.A.; Snurr, R.Q.; Hupp, J.T.; Farha, O.k. A facile synthesis of UiO-66, UiO-67 and their derivatives. *Chem. Commun.* **2013**, *49*, 9449–9451. [CrossRef]
30. Cavka, J.H.; Jakobsen, S.; Olsbye, U.; Guillou, N.; Lamberti, C.; Bordiga, S.; Lillerud, K.P. A New Zirconium Inorganic Building Brick Forming Metal Organic Frameworks with Exceptional Stability. *J. Am. Chem. Soc.* **2008**, *130*, 13850–13851. [CrossRef]
31. Tian, N.; Huang, H.; Liu, C.; Dong, F.; Zhang, T.; Du, X.; Yu, S.; Zhang, Y. In situ co-pyrolysis fabrication of CeO_2/g-C_3N_4 n–n type heterojunction for synchronously promoting photo-induced oxidation and reduction properties. *J. Mater. Chem. A* **2015**, *3*, 17120–17129. [CrossRef]
32. Wen, X.-J.; Niu, C.-G.; Zhang, L.; Liang, C.; Zeng, G.-M. A novel Ag_2O/CeO_2 heterojunction photocatalysts for photocatalytic degradation of enrofloxacin: Possible degradation pathways, mineralization activity and an in depth mechanism insight. *Appl. Catal. B Environ.* **2018**, *221*, 701–714. [CrossRef]
33. Zhang, X.; Zhang, N.; Gan, C.; Liu, Y.; Chen, L.; Zhang, C.; Fang, Y. Synthesis of In_2S_3/UiO-66 hybrid with enhanced photocatalytic activity towards methyl orange and tetracycline hydrochloride degradation under visible-light irradiation. *Mater. Sci. Semicond. Process.* **2019**, *91*, 212–221. [CrossRef]
34. Zhu, G.; Feng, S.; Chao, J.; Zheng, W.; Shao, C. One-pot synthesis of C-dots modified TiO_2 nanosheets/UiO-66-NH_2 with improved photocatalytic activity under visible light. *Ceram. Int.* **2019**, *46*, 2530–2537. [CrossRef]
35. Lee, D.T.; Zhao, J.; Oldham, C.J.; Peterson, G.W.; Parsons, G.N. UiO-66-NH_2 Metal–Organic Framework (MOF) Nucleation on TiO_2, ZnO, and Al_2O_3 Atomic Layer Deposition-Treated Polymer Fibers: Role of Metal Oxide on MOF Growth and Catalytic Hydrolysis of Chemical Warfare Agent Simulants. *ACS Appl. Mater. Interfaces* **2017**, *9*, 44847–44855. [CrossRef]
36. Saravanakumar, K.; Ramjan, M.M.; Suresh, P.; Muthuraj, V. Fabrication of highly efficient visible light driven Ag/CeO_2 photocatalyst for degradation of organic pollutants. *J. Alloy. Compd.* **2016**, *664*, 149–160. [CrossRef]
37. Pan, Y.; Yuan, X.; Jiang, L.; Wang, H.; Yu, H.; Zhang, J. Stable self-assembly AgI/UiO-66(NH_2) heterojunction as efficient visible-light responsive photocatalyst for tetracycline degradation and mechanism insight. *Chem. Eng. J.* **2020**, *384*, 123310. [CrossRef]
38. Bariki, R.; Majhi, D.; Das, K.; Behera, A.; Mishra, B. Facile synthesis and photocatalytic efficacy of UiO-66/$CdIn_2S_4$ nanocomposites with flowerlike 3D-microspheres towards aqueous phase decontamination of triclosan and H2 evolution. *Appl. Catal. B Environ.* **2020**, *270*, 118882. [CrossRef]
39. Zhang, L.; Hu, C.; Ji, H. p-AgI anchored on {001} facets of n-$Bi_2O_2CO_3$ sheets with enhanced photocatalytic activity and stability. *Appl. Catal. B Environ.* **2017**, *205*, 34–41. [CrossRef]
40. Cho, H.D.; Yoon, I.T.; Chung, K.B.; Kim, D.Y.; Kang, T.W.; Yuldashev, S. Low-temperature photoluminescence of WO_3 nanoparticles. *J. Lumin.* **2018**, *195*, 344–347. [CrossRef]
41. Wu, X.; Yuan, G.; Zeng, L.; Jiang, H.; Zhong, Y.; Xie, H.; Wang, X.; Chen, H. Wang, Highly efficient photocatalytic activity and mechanism of Yb^{3+}/Tm^{3+} codoped In_2S_3 from ultraviolet to near infrared light towards chromium (VI) reduction and rhodamine B oxydative degradation. *Appl. Catal. B Environ.* **2018**, *225*, 8–21. [CrossRef]
42. Zhang, J.; Qiao, S.Z.; Qi, L.; Yu, J. Fabrication of NiS modified CdS nanorod p–n junction photocatalysts with enhanced visible-light photocatalytic H_2-production activity. *Phys. Chem. Chem. Phys.* **2013**, *15*, 12088–12094. [CrossRef] [PubMed]

43. Wen, J.; Li, X.; Li, H.; Ma, S.; He, K.; Xu, Y.; Fang, Y.; Liu, W.; Gao, Q. Enhanced visible-light H_2 evolution of g-C3N4 photocatalysts via the synergetic effect of amorphous NiS and cheap metal-free carbon black nanoparticles as co-catalysts. *Appl. Surf. Sci.* **2015**, *358*, 204–212. [CrossRef]
44. Deng, Y.; Tang, L.; Zeng, G.; Feng, C.; Dong, H.; Wang, J.; Feng, H.; Liu, Y.; Zhou, Y.; Pang, Y. Plasmonic resonance excited dual Z-scheme $BiVO_4$/Ag/Cu_2O nanocomposite: Synthesis and mechanism for enhanced photocatalytic performance in recalcitrant antibiotic degradation. *Environ. Sci. Nano* **2017**, *4*, 1494–1511. [CrossRef]